Journal of Materials Chemistry A

ROYAL SOCIETY OF CHEMISTRY

PAPER

View Article Online
View Journal | View Issue

Cite this: J. Mater. Chem. A, 2025, 13, 36140

Elucidating Ti dopant effects in hematite photoanodes *via* high-throughput combinatorial screening

Marco Salvi, [a] Alberto Piccioni,[ab] Nicola Gilli,[b] Alessandro Puri,[ac] Federico Boscherini, [ad] Raffaello Mazzaro *[ab] and Luca Pasquini [ab]

Hematite (α-Fe_2O_3) represents a promising candidate for photoelectrochemical water splitting, but its practical application is hindered by poor charge transport and sluggish surface kinetics. Despite extensive research on titanium doping as a performance enhancer, the underlying mechanisms remain debated, with widely varying optimal concentrations reported across different fabrication techniques. Here, we demonstrate how high-throughput combinatorial approaches can rapidly elucidate complex structure–function relationships that would be challenging to identify through conventional methods. We first optimize titanium content using a concentration gradient sample, then leverage this optimal composition to create two complementary sample types: one with titanium co-sputtered throughout the hematite film and another with titanium sequentially deposited as an overlayer. By subjecting both sample types to similar temperature gradients, we create a powerful comparative framework that reveals how the same elements behave differently based on initial spatial distribution, yet converge toward similar structures at higher temperatures. This parallel temperature evolution allows us to precisely identify the conditions where performance dramatically changes and target these specific regions for in-depth structural characterization. Our findings reveal that Ti enhances photoactivity through two pathways: modifying surface properties to improve charge transfer efficiency and acting as a substitutional dopant to increase bulk charge separation. Structural analysis confirms titanium incorporates into hematite up to a thermodynamic solubility limit of approximately 4–5% Ti/(Ti + Fe), with excess titanium segregating to form surface TiO_2 phases that become detrimental beyond optimal thickness. This comparative gradient approach represents a powerful strategy for simultaneously optimizing materials while unlocking fundamental mechanistic insights that are difficult to gain by means of conventional single-parameter studies.

Received 23rd May 2025
Accepted 19th September 2025

DOI: 10.1039/d5ta04174k

rsc.li/materials-a

[a]Department of Physics and Astronomy, Alma Mater Studiorum – Università di Bologna, Viale Berti Pichat 6/2, 40127 Bologna, Italy. E-mail: raffaello.mazzaro@unibo.it

[b]CNR - Istituto per lo Studio dei Materiali Nanostrutturati (ISMN), Via P. Gobetti 101, 40129 Bologna, Italy

[c]CNR - Istituto Officina dei Materiali (IOM), Grenoble c/o ESRF, The European Synchrotron, 71 Avenue des Martyrs, CS40220, 38043 Grenoble Cedex 9, France

[d]CNR - Istituto Officina dei Materiali (IOM), c/o AREA Science Park Basovizza, SS 14, Km 163.5, 34149 Trieste, Italy

R. Mazzaro

Dr Raffaello Mazzaro is an Assistant Professor in the Department of Physics and Astronomy (DIFA) at the University of Bologna. He obtained his PhD in Chemistry in 2016 and subsequently held postdoctoral research positions at the National Research Council of Italy (CNR) and Luleå University of Technology in Sweden. He later joined the Nanomaterials for Energy Conversion and Storage (N-REX) group at DIFA, where he currently leads research activities focused on unraveling structure–function relationships in materials for solar energy conversion and solar-driven chemical transformations. Dr Mazzaro's interdisciplinary research spans chemistry, materials science, and condensed matter physics, with the overarching goal of enabling the rational design of advanced functional materials for sustainable energy technologies.

Introduction

Photoelectrochemistry (PEC) is widely regarded as a promising route for sustainable hydrogen production. Despite extensive research into a wide range of compositions, structures, and morphologies, the parameter space for PEC materials remains largely unexplored due to the inherently low throughput of conventional investigation methods. High-throughput preparation (HTP) and high-throughput screening (HTS) provide efficient strategies for identifying materials that meet key performance criteria. Several studies have applied these approaches to PEC applications, particularly focusing on the development of metal oxide photoanodes for the oxygen evolution reaction (OER). A common strategy involves the deposition of a lateral stoichiometric gradient of a ternary oxide, enabling the exploration of all intermediate metal ratios, from dilute doping regimes to fully stoichiometric ternary compounds. This can be achieved through several deposition technologies including inkjet printing,[1,2] sputtering[3,4] and electrodeposition.[5] Notable examples include Fe–W–O,[6] Fe–Ti–O,[7] Ag–V–O[8] or Cu–V–O[9] systems, where minor adjustments in metal composition have led to significant enhancements in PEC performance. More complex libraries incorporating orthogonal gradients have also been used to vary additional parameters, such as the inclusion of a fourth element[4,10,11] or a thickness variation.[12] This promising approach is however still underutilized, as hardly any attempt is reported to develop deposition with *e.g.* (i) an orthogonal temperature gradient, possibly resulting in phase transitions,[13] (ii) a gradient in the gaseous environment (*e.g.* increasing O_2/Ar or N_2/Ar ratio[14]) (iii) pressure gradients altering plasma supersaturation.[15]

Hematite is one of the most studied candidates photoanodes for water splitting due to its bandgap of around 2–2.2 eV, its valence band positioning relative to the OER redox potential, its stability and the abundance of its constituent elements. However, its practical performance is limited by poor charge transport properties and sluggish surface kinetics. Various strategies have been proposed to overcome these limitations,[16] with aliovalent doping, such as titanium incorporation, being one of the most widely explored. Yet, the mechanisms through which Ti enhances PEC performance remain debated. Some studies attribute its effects to conventional substitutional doping,[17,18] while others report influences on surface properties[19,20] or also on both these aspects.[21] Furthermore, the optimal Ti concentration often varies depending on the fabrication method,[19,21–24] complicating the transfer of knowledge across different synthesis approaches. As a result, optimization of the dopant level is frequently required for each new deposition strategy.

Another important parameter that is more overlooked is the annealing temperature.[17] Many fabrication methods indeed rely on a post deposition temperature treatment that can help in the crystallization of the hematite and in its oxidation. These thermal treatments can be informed by phase diagrams, but ultimately often rely on practice.

In this work we study both doping and annealing temperature in magnetron sputtered Ti doped hematite. In particular, we show how high throughput methodologies can not only be employed for the optimization of such parameters, which has already been shown before for dopant concentration,[25,26] but also to select the values of these parameters where the change in performance happens for deeper investigation. These values are indeed the ones that are worthy of being investigated with more time-consuming structural measurements that can explain what physical or chemical features are responsible for an improved photocurrent.

Experimental

Materials and methods

The substrates used are fluorine doped tin oxide (FTO) covered glass substrates that have been cut to the desired shape and size using an Odin 32 laser cutter from Thunder Laser. The hematite films were deposited by RF magnetron sputtering starting from a 2″ hematite target with a power of 40 W. Titanium was deposited through DC magnetron sputtering of a 2″ titanium target. All depositions have been performed starting from a pressure of around 5×10^{-7} mbar and adding 10 sccm of Ar gas to reach a pressure of 8×10^{-3} mbar. Thermal treatments for the samples undergoing gradient annealing have been performed in a multi-zone tube furnace atmosphere, calibrated with a thermocouple along the tube axis, to determine the precise local temperature. Annealing for concentration gradient samples was performed in a muffle furnace. The samples were inserted in the furnace when it had already reached the desired temperature and taken out after 10 minutes to cool at room temperature. This fast sample insertion process was chosen to minimize FTO degradation.[17]

Thickness calibrations and surface morphology images were performed using a Zeiss Leo 1530 Field Emission Scanning Electron Microscope (FE-SEM), operated at 5 kV and equipped with in-lens secondary electrons detector.

All photoelectrochemical measurements have been conducted using a custom scanning photoelectrochemical flow cell (SPFC). The SPFC is described in the SI. In short, the cell confines the measurement area to a circle with a diameter of 1.5 mm, and sequentially probes the desired spots on each sample, corresponding to a specific sample configuration, either differing by composition or annealing temperature. The potentiostat used is an Autolab PGSTAT 204 potentiostat equipped with a Frequency Response Analyzer module (FRA). The reference electrode was an Ag/AgCl with NaCl 3 M from ALS Japan and the counter electrode a Pt wire. Light was provided through a UV LED with a wavelength of 385 nm (THORLABS M385FP1). For the LSV measurements the intensity was 20 mW cm^{-2} whereas for the Intensity Modulated Photocurrent Spectroscopy (IMPS) measurements we used a 16.5 mW cm^{-2} DC intensity and added an AC intensity modulation which had an RMS amplitude of 10% of the DC part. Additional LSV measurements have been performed in blue light at 455 nm (THORLABS M455F3) with an intensity of 26.8 mW cm^{-2} and in white light (THORLABS MCWHF2). The light intensity has been calibrated using an Hamamatsu S2281-01. The electrolyte was NaOH 0.1 M (pH 12.8) with the addition of Na_2SO_4 0.5 M

supporting electrolyte to increase the conductivity. All measurements have been performed with front illumination.

The structure of specific points of interest identified from the high throughput photoelectrochemical measurements was investigated through Transmission Electron Microscopy (TEM), X-ray Diffraction (XRD), UV-Vis absorbance spectroscopy and X-ray Absorption Spectroscopy (XAS) measurements.

TEM specimens where prepared using a Zeiss Crossbeam 340 (SEM/FIB). Cross-section TEM lamellae were lifted out using a Ga-focused ion beam operating at 30 keV after the deposition of a Pt protection layer over the region of interest using a gas-injection system (GIS). The lamellae were then thinned to a thickness of approximately 80 nm, followed by a final polishing step at 5 keV for reduced amorphization. TEM measurements were conducted with a FEI Tecnai F20 ST S/TEM, operating with a nominal accelerating voltage of 200 kV, equipped with energy dispersive X-ray system (EDS). EDS elemental mapping was performed with a Thermo Fisher Talos F200S G2 S-FEG operating at 200 keV equipped with two window-less EDS detectors.

XRD measurements have been performed using an Empyrean diffractometer from Malvern Panalytical equipped with a Cu anode operated at 40 kV and 40 mA. All measurements have been performed in a Bragg–Brentano geometry with a divergence slit of $\frac{1}{4}$ and two masks controlling the lateral divergence of the beam set both with an aperture of 2 mm. The irradiated area had a FWHM of 3.7 mm. The highest temperature variation inside such an area is 20 °C.

Absorbance measurements were performed using an Agilent Cary 5000 UV-Vis-NIR Spectrophotometer. Absorbance has been calculated by measuring reflectance and transmittance using an integrating sphere and applying the formula $-\log_{10}(T + R)$.

XAS measurements at the Ti K-edge (4965 eV) have been performed at the LISA-BM08 CRG beamline[27] of the European Synchrotron Radiation Facility (ESRF). The samples have been inserted into a chamber where vacuum was created to minimize the beam absorption from air molecules. X-ray radiation is selected using a sagittal Si 111 Double Crystal Monochromator (DCM), producing a beam size on the sample of approximately 100 μm × 100 μm. The dependence of the X-ray absorption coefficient on the energy of the incident photon was determined by detecting the fluorescence photons, as the glass substrate was too thick to work in transmittance. To maximize the signal from the film, the measurement has been made in grazing incidence. X-ray fluorescence intensity at the Ti-Kα was registered with a 12-element high-purity Ge detector and normalized to the incident X-ray beam intensity.

Samples fabrication

Three kinds of samples have been prepared as summarized in Fig. 1 and discussed more in detail in the SI. First, a sample with a homogeneous hematite film and a titanium overlayer of varying thickness on top of it, which was flash-annealed at 750 °C, so that Ti could diffuse in the hematite lattice. The thickness gradient was obtained by reducing the distance between the target and the sample during the sputtering of Ti and holding the sample holder stationary, taking inspiration from previous works to fabricate compositional materials libraries using magnetron sputtering.[3,28] One zone of the sample was masked before the Ti deposition to have a reference point with no dopant (see Fig. S1). This sample was used to find an optimal amount of Ti and will be referred to as Ti:Fe_2O_3|ΔTi. Subsequently, four additional samples were prepared. Two of these were fabricated by depositing a homogeneous Ti layer of the previously optimized thickness on top of the hematite film. These samples will be referred to as Ti:Fe_2O_3|Δ*T*-seq. The other two have been made by co-sputtering hematite and titanium, using the same amount of titanium as for Ti:Fe_2O_3|Δ*T*-seq.

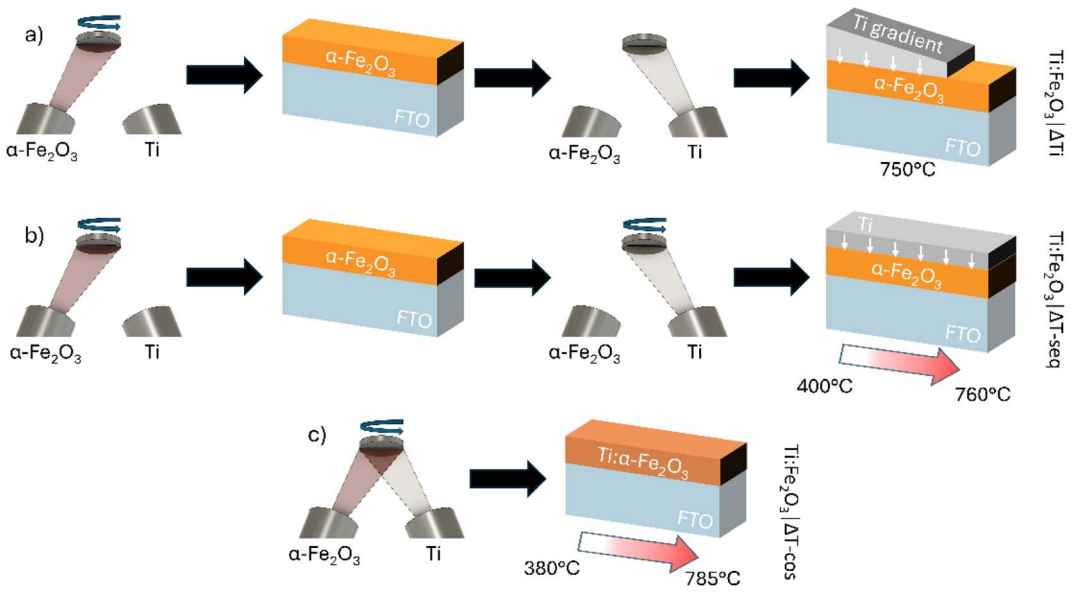

Fig. 1 Schematic depiction of the fabrication steps for the three different kinds of samples analysed in the study: (a) Ti:Fe_2O_3|ΔTi; (b) Ti:Fe_2O_3|Δ*T*-seq and (c) Ti:Fe_2O_3|Δ*T*-cos.

These will be referred to as Ti:Fe_2O_3|Δ*T*-cos. All these samples have then been flash annealed (10 min) with a gradient of temperature, as shown in Fig. 1, in order to avoid FTO degradation issues. These would have interfered with the cross-correlation of structural and functional properties related to the active material. The reported annealing temperatures for these samples are thus to be considered in the context of such a short annealing and the results are not to be generalized to longer treatments.

Results and discussion

Photoelectrochemical characterization

Linear sweep voltammetries under UV light for the Ti:Fe_2O_3|ΔTi sample are shown in Fig. 2a. In Fig. 2b the corresponding photocurrent values at 1.6 V *vs.* RHE are plotted as a function of the thickness of the sputtered Ti overlayer. The top horizontal axis reports the corresponding Ti content expressed in Ti/(Fe + Ti) (%). These have been reported to comply with the usual way of referring to doping in literature, although these nominal values differ from the actual local Ti concentration, as later discussed. It can be seen that the photocurrent increases with increasing thickness of the Ti layer, up to a maximum value of about 250 μA cm^{-2} at 14.7 nm. The corresponding nominal Ti content value, equal to 12.3% Ti/(Ti + Fe), was employed for the fabrication of the samples undergoing the annealing in temperature gradient. It is worth noting that hematite without titanium shows almost no photocurrent, which has already been observed for samples prepared through other fabrication strategies.[23] This seems to be independent of the wavelength employed, as the same effect was observed under blue (Fig. S5) and white (Fig. S7) light. Fig. 3 shows linear sweep voltammetries under light for the temperature gradient samples (Ti:Fe_2O_3|Δ*T*-seq and Ti:Fe_2O_3|Δ*T*-cos). In Ti:Fe_2O_3|Δ*T*-seq, the onset of significant photocurrent occurs at higher annealing temperatures. Indeed, if considering the photocurrent at 750 °C as maximum saturation current, half of this value was reached at 700 °C, while the same value was reached at 500 °C in Ti:Fe_2O_3|Δ*T*-cos. Additionally, the rise in photocurrent with temperature is gradual on Ti:Fe_2O_3|Δ*T*-cos, whereas Ti:Fe_2O_3-|Δ*T*-seq exhibits a sudden jump between ~700 °C and ~720 °C. Similar trends of the photocurrent have been observed also in blue (Fig. S6) and white light (Fig. S8).

To deconvolve the contributions of interfacial charge transfer and bulk charge separation on the performance of the material we performed IMPS measurements. The resulting spectra (Fig. S9) have been fitted with a distribution of relaxation time (DRT) thanks to an algorithm reported previously by our group.[29] In this way it is possible to extract from these measurements the relevant figures of merit for the semiconductor's charge carrier dynamics. Details on the calculations can be found in the SI. In particular, here we will comment:

(i) The current density j_G associated to photogenerated minority carriers that survive bulk recombination and accumulate at the interface with the electrolyte, given by:

$$j_G = eI_0 \times \mathrm{CSE} \times \mathrm{LHE}$$

where I_0 is the incident power per unit area (W cm^{-2}), CSE is the charge separation efficiency, LHE is the light harvesting efficiency. The first analytical model for j_G is the one developed by Gärtner[30] which has later been refined by other authors.[31] However, our analysis does not rely on a specific analytical model to determine j_G (see SI).

(ii) The charge transfer efficiency η_{trans}, which represents the fraction of minority carriers that gets transferred into the solution.

In this perspective, the final photocurrent density can be factorized as $j_{photo} = j_G\eta_{trans}$

To further deconvolve the contribution of charge separation efficiency from the one of light harvesting in j_G, reflectance and transmittance measurements were performed in order to compute the absorbance at the wavelength of interest (Fig. S14). Fig. 4 shows the normalized j_{photo} and j_G and the transfer efficiency η_{trans}, evaluated at 1.45 V *vs.* RHE for varying Ti amount and annealing temperature. This potential was chosen for the

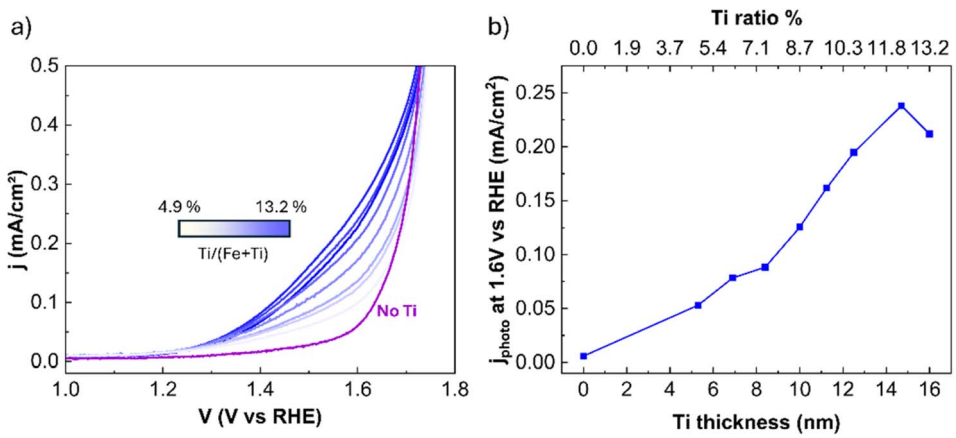

Fig. 2 (a) Linear sweep voltammetries under UV illumination for the Ti:Fe_2O_3|ΔTi sample: the one on the point with no titanium is coloured in purple. (b) Photocurrents at 1.6 V *vs.* RHE at different Ti content for the sample: the photocurrents have been computed subtracting the value of current for the LSV in the dark at that potential from the one under illumination.

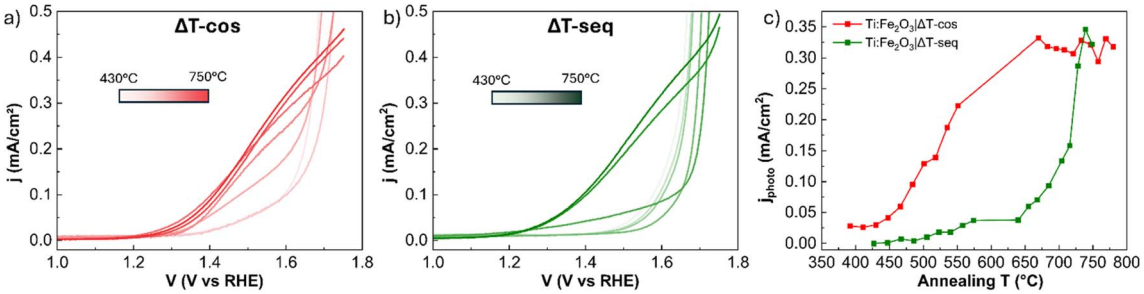

Fig. 3 (a and b) Linear sweep voltammetries under UV illumination for the temperature gradient samples at selected representative temperatures of 430 °C, 470 °C, 500 °C, 550 °C, 670 °C, 720 °C and 750 °C: (a) Ti:Fe_2O_3|Δ*T*-cos and (b) Ti:Fe_2O_3|Δ*T*-seq (c) comparison of photocurrents at different *T* on the two samples at 1.6 V *vs.* RHE: the photocurrents have been computed subtracting the value of current for the LSV in the dark at that potential from the one under illumination.

comparison to avoid overlapping contribution of dark OER, unavoidable at larger potentials for the low-*T* annealed regions of the *T*-gradient samples.

In the Ti:Fe_2O_3|ΔTi, the addition of Ti increases the transfer efficiency compared to the bare hematite. The transfer efficiency remains almost constant up to 10% Ti/(Ti + Fe), then it decreases slightly. j_G on the other hand reaches a maximum that coincides with the maximum of the photocurrent and then decreases. This change in j_G can be attributed purely to a change in charge separation efficiency, as the absorbance at the wavelength employed for IMPS is independent of Ti content. For Ti:Fe_2O_3|Δ*T*-cos, the transfer efficiency rises between approximately 450 °C and 550 °C, after which it remains approximately constant. Meanwhile, j_G continues to increase up to around 670 °C, following the same trend observed for the photocurrent. For this sample the rise in j_G between 400 °C and 500 °C could be justifiable purely with an increase in charge separation efficiency. On the other hand, since the absorbance seems to increase between 500 °C and 750 °C, in this temperature range increased photon capitalization could also play a role.

In Ti:Fe_2O_3|Δ*T*-seq, instead, the transfer efficiency increases between 550 °C and 700 °C and then decreases, when j_{photo} and j_G are still negligible, while the latter suddenly increases above 700 °C. Here absorbance shows little change with increasing temperature and the charge separation efficiency is thus responsible for the change in j_G.

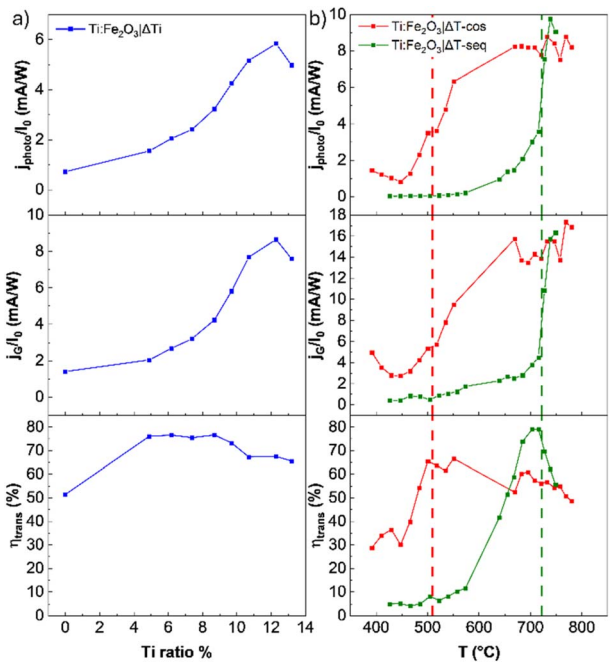

Fig. 4 Normalized photocurrent (upper frames), normalized j_G (central frames) and transfer efficiency (lower frames) obtained by fitting IMPS data acquired at 1.45 V *vs.* RHE with a DRT algorithm for (a) Ti:Fe_2O_3|ΔTi, (b) Ti:Fe_2O_3|Δ*T*-cos and Ti:Fe_2O_3|Δ*T*-seq. The lines mark the points of highest derivative for the photocurrents.

Structural characterization

To gain microscopic insight into the trends observed in PEC performance, structural characterization was performed on selected regions of Ti:Fe_2O_3|Δ*T*-cos and Ti:Fe_2O_3|Δ*T*-seq. XRD profiles are shown in Fig. 5a and c. Hematite peaks are indexed with the corresponding Miller indexes. Additional peaks are attributed to the FTO substrate. In Ti:Fe_2O_3|Δ*T*-seq three hematite peaks are visible in the investigated angular range for all temperatures tested. Orientation along the (110) plane is generally considered more beneficial for photoelectrochemical performance, as electron mobility is higher along the direction perpendicular to this crystalline plane.[32] A common way to assess the degree of preferential orientation is to compare it to the one of the (104) direction.[23] To investigate the structural evolution as a function of temperature, Rietveld refinement was conducted on the two characteristic diffraction peaks. The results are summarized in Table S1. The analysis indicates a clear increase in crystallite size with increasing annealing temperature, particularly along the (104) crystallographic orientation, as illustrated in Fig. 5b and d. Fig. S15 presents the evolution of the intensity ratio between the (104) and (110) reflections, which increases progressively with temperature. This suggests a temperature-induced shift in preferential orientation. While such a shift may be adverse for certain material properties, the concurrent enhancement in crystallite size could be advantageous, as it is likely to reduce the density of defects typically associated with grain boundaries.

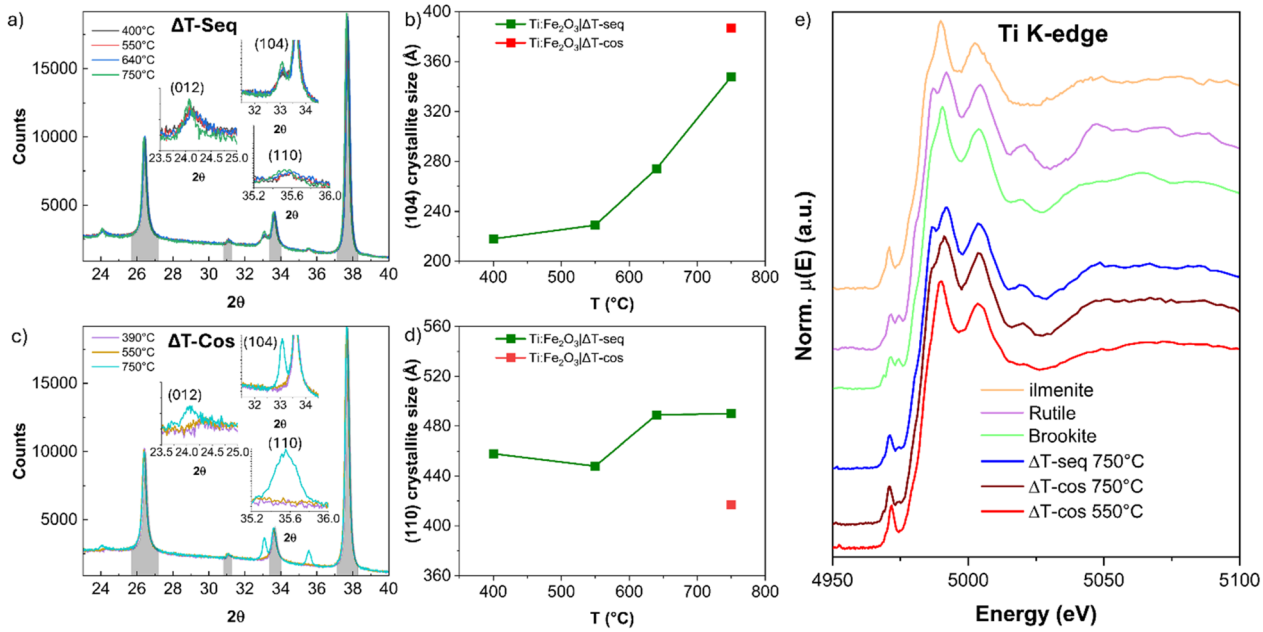

Fig. 5 XRD profiles for the two gradient T samples at different temperatures (a) Ti:Fe_2O_3|ΔT-seq and (c) Ti:Fe_2O_3|ΔT-cos. Peaks corresponding to hematite crystalline planes are highlighted with the corresponding Miller indexes, whereas FTO peaks are highlighted in gray. (b and d) (104) and (110) crystallite sizes *vs.* temperature. (e) XAS spectra of Ti:Fe_2O_3|ΔT-seq at 750 °C, Ti:Fe_2O_3|ΔT-cos at 750 °C and 550 °C and of some reference samples in known phases.

In contrast, for Ti:Fe_2O_3|ΔT-cos, hematite diffraction peaks are observed only after annealing at 750 °C, suggesting that the film remains either amorphous or nanocrystalline with extremely fine grains at lower temperatures. This observation implies that the incorporation of titanium during the sputtering process suppresses the crystallization of hematite. The crystallization at higher temperatures could explain the increase in absorbance between 500 °C and 750 °C. Despite this, a substantial increase in photocurrent is already evident between 390 °C and 550 °C, where no crystalline feature is observed. Notably, the intensity ratio of the (104) to (110) reflections at 750 °C is lower for Ti:Fe_2O_3|ΔT-cos compared to Ti:Fe_2O_3|ΔT-seq, even though both exhibit nearly identical photoelectrochemical performance and IMPS-derived parameters in UV light. On the other hand, in white light (Fig. S8) Ti:Fe_2O_3|ΔT-seq shows considerably more photocurrent than Ti:Fe_2O_3|ΔT-cos at high temperatures. While these results might seem in contrast, it is possible that for carriers generated by high energy photons, high mobility directions like (110) become less important, since the excess energy can be given to the lattice to break the polaron that usually slows down charge carriers in hematite.[33] This result suggests that the mechanism of inclusion of titanium and its effect on crystallization could actually be relevant in the performance.

XRD was not able to detect any Ti-rich phase in both types of samples even after high-temperature annealing, probably because of its small amount or poor crystallinity. Therefore, Ti K-edge XAS has been used to study the local structure of titanium. Fig. 5e shows the XANES collected from the 750 °C points of both Ti:Fe_2O_3|ΔT-seq and Ti:Fe_2O_3|ΔT-cos, along with the 550 °C point from the latter. The spectra have been fitted with a linear combination of the spectra of reference anatase, brookite, ilmenite and rutile (see Fig. S16 and Table S2). For clarity, only the reference phases with the highest contributions are shown in Fig. 5e. The point at 550 °C on Ti:Fe_2O_3|ΔT-cos shows the presence of an ilmenite phase together with brookite. At high temperature, the Ti-rich phase of both samples is well described by a combination of rutile and brookite.

SEM analysis (Fig. S17) of Ti:Fe_2O_3|ΔT-seq and Ti:Fe_2O_3|ΔT-cos samples does not reveal any noticeable change in surface morphology as a function of the annealing temperature or the Ti inclusion method. Instead, on Ti:Fe_2O_3|ΔTi sample a slight decrease in surface roughness is observed upon addition of Ti.

FIB lamellae for TEM observations have been prepared for the points at 390 °C, 550 °C and 750 °C on Ti:Fe_2O_3|ΔT-cos and the ones at 640 °C and 750 °C on Ti:Fe_2O_3|ΔT-seq. These points have been chosen because, as shown in Fig. 6a, they marked relevant transitions in the performance of the sample, whose behaviour could not be explained by XRD alone. Fig. 6 also shows EDS profiles that have been acquired moving from the surface to the substrate.

In Ti:Fe_2O_3|ΔT-cos, zones annealed at 550 °C and 390 °C show a rather homogeneous and smoothly varying Ti content across the film thickness of around 7–8% local Ti/(Ti + Fe) ratio (Fig. 6d and e). Interestingly, after annealing at 750 °C, the Ti content inside the hematite grains decreases to around 4.5% local Ti/(Fe + Ti) ratio (Fig. 6f), while regions with higher Ti content emerge in correspondence of the inner grain boundaries and of the film surface, suggesting the segregation of a Ti-rich phase.

Ti:Fe_2O_3|ΔT-seq, instead, at 640 °C exhibits a high Ti content on the surface, indicative of the titanium overlayer, and

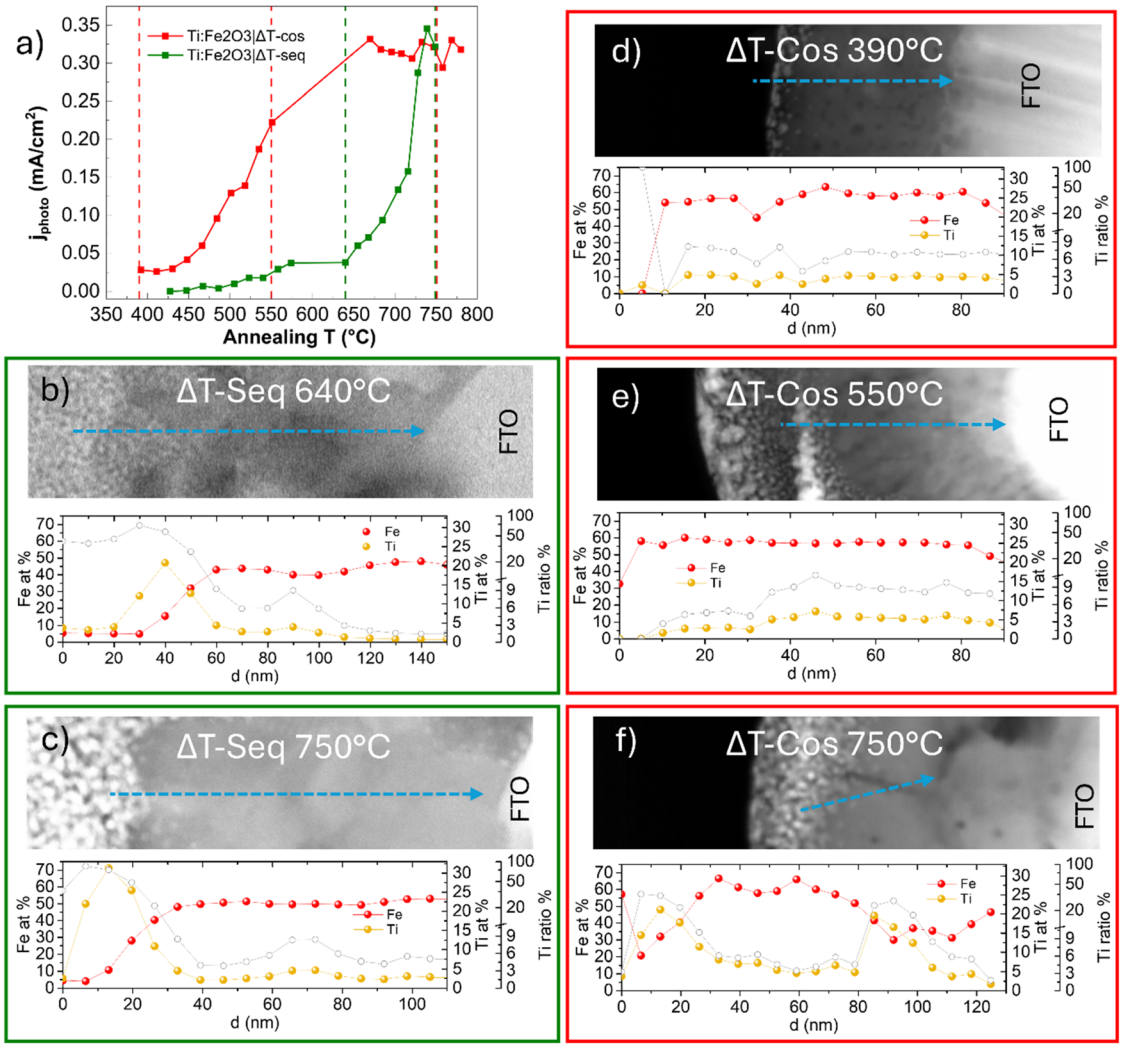

Fig. 6 TEM EDS profiles made on points at different temperatures on Ti:Fe_2O_3|Δ*T*-cos and Ti:Fe_2O_3|Δ*T*-seq, following the blue dashed arrow. The Ti/(Fe + Ti)% ratio is also shown. (b and c) Ti:Fe_2O_3|Δ*T*-seq at 640 °C and 750 °C, (d–f) Ti:Fe_2O_3|Δ*T*-cos at 390 °C, 550 °C and 750 °C, (a) photocurrent plots with lines highlighting the relevance of the chosen temperatures. High contrast nanoparticles on the surface of the hematite layer are due to Pt protection layer, required for FIB lamella preparation.

a diffusion like titanium profile in the hematite film which decreases down to 2% local Ti/(Ti + Fe) ratio far from the surface. Moving to 750 °C the Ti content in the film becomes more homogeneous and increases to approximately 4% local Ti/(Ti + Fe) ratio. This difference evidently originates with Ti diffusion from the overlayer into hematite bulk that occurs appreciably between these two temperatures. Even at the highest annealing temperature, an excess titanium content is detected at the surface, where Fe content is very low. Therefore, the surface layers may be related with TiO_2 phases such as rutile and brookite detected *via* XAS.

Elemental maps have been acquired to highlight the redistribution of Ti in Ti:Fe_2O_3|Δ*T*-cos and Ti:Fe_2O_3|Δ*T*-seq at high temperature (Fig. 7). The elemental maps show quite clearly that titanium accumulates at the grain boundaries and at the surface in Ti:Fe_2O_3|Δ*T*-cos. They also show a Ti-rich film at the surface of Ti:Fe_2O_3|Δ*T*-seq. EDS quantification over a rectangular region inside a hematite grain reveals that the Ti contents of the two samples after annealing at 750 °C are very close, with 4.2% local Ti/(Ti + Fe) and 4.1% local Ti/(Ti + Fe) in Ti:Fe_2O_3|Δ*T*-cos and Ti:Fe_2O_3|Δ*T*-seq, respectively (see Fig. S18 and Table S3). This similarity suggests that a solubility limit is approached in both cases. In Ti:Fe_2O_3|Δ*T*-cos, the excess titanium must diffuse out of the hematite grains towards the grain boundaries and the surface. In Ti:Fe_2O_3|Δ*T*-seq, Ti diffuses from the surface layer into the hematite grains until the solubility threshold is reached. The excess titanium in both cases seems to restructure as titanium dioxide in the form of rutile and brookite, as pointed out by XAS and confirmed by HRTEM images, which show a phase with lattice spacing compatible with the one of rutile on top of the point at 750 °C on Ti:Fe_2O_3|Δ*T*-cos (see Fig. S20).

This observation is coherent with the work of Morante *et al.*[21] who found the presence of pseudobrookite and rutile segregation at doping of 20%. Ti and suggested that pseudobrookite formation may begin already at 5%. A phase study on the TiO_2–

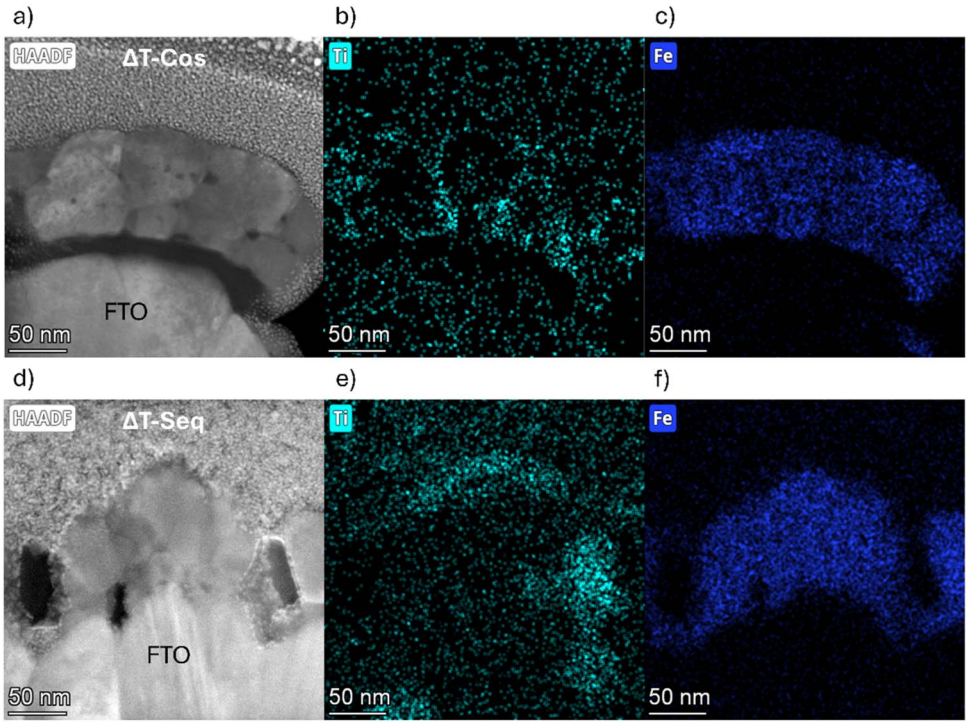

Fig. 7 TEM images and elemental maps. (a) image, (b) Ti and (c) Fe elemental maps for the point at 750 °C on Ti:Fe_2O_3|Δ*T*-cos; (d) image, (e) Ti and (f) Fe elemental maps for a point at 750 °C on Ti:Fe_2O_3|Δ*T*-seq.

Fe_2O_3 system, instead, found a limit of solubility of the former in the latter of ~9.5% Ti ratio for a preparation temperature of 1000 °C.[34] While this is above the 4% solubility limit found by us, our samples were annealed at lower temperatures, and that same study noted a decrease in solubility with decreasing temperature. Besides, as already stressed, EDS measurements are not perfectly quantitative, and attention should be focused more on the relative similarity in Ti content between the two samples than on the absolute values. Similar EDS measurements mediated inside the area of a grain for Ti:Fe_2O_3|Δ*T*-seq at 640 °C found a Ti ratio of 1.1% local Ti/(Ti + Fe), confirming the diffusion is not complete at this temperature. Another aspect we investigated using EDS is the diffusion of Sn, as Sn diffusing from the FTO substrate is sometimes considered another potential dopant. As can be seen in Table S3, the amount of Sn does not seem to vary significantly between 640 °C and 750 °C on Ti:Fe_2O_3|Δ*T*-seq, where the biggest jump in photocurrent happens. The amount detected is also small over all temperatures tested and maybe it is not reliable given the limitations of EDS in the detection of small elemental components. The biggest evidence for a lack of a significant role of Sn diffusion on the performance though comes from Ti:Fe_2O_3|ΔTi. Here, indeed, the point with no titanium shows negligible photocurrent even if it is annealed at the same temperature as all the other ones and the change in performance seems purely affected by the presence of Ti.

Besides the redistribution of titanium, we investigated structure and crystallinity using High Angle Annular Dark Field Scanning Transmission Electron Microscopy (HAADF-STEM) and High-Resolution Transmission Electron Microscopy (HRTEM). As shown in Fig. S19 the structure of Ti:Fe_2O_3|Δ*T*-cos evolves from a compact block at 390 °C to a well-defined assembly of crystalline grains at 750 °C. Further magnified HRTEM in Fig. S20 reveal that the size of the crystalline domains increases with temperature in both samples. The Fast Fourier Transforms reveal the presence of hematite already at 550 °C in Ti:Fe_2O_3|Δ*T*-cos, where XRD had failed to show any peaks. In this sample it is likely that crystallization needs a higher temperature because the excess titanium atoms in the film need to be expelled for the structure to rearrange.

Discussion

In this section, we correlate structural characterization with photoelectrochemical performance to elucidate the role of titanium in enhancing hematite activity. The resulting concepts emerging from this discussion are schematically summarized in (Fig. 8). We begin with an analysis of j_G and subsequently address surface-related effects such as charge transfer efficiency.

In Ti:Fe_2O_3|Δ*T*-seq, a notable increase in j_G is observed only at higher annealing temperatures (>700 °C) while absorbance remains consistent. This behavior is consistent with the requirement for titanium atoms to thermally diffuse into the hematite lattice in order to function effectively as dopants and suggests that doping affects charge separation efficiency. Indeed, transmission electron microscopy (TEM) analysis confirms that Ti diffusion remains incomplete at 640 °C, where

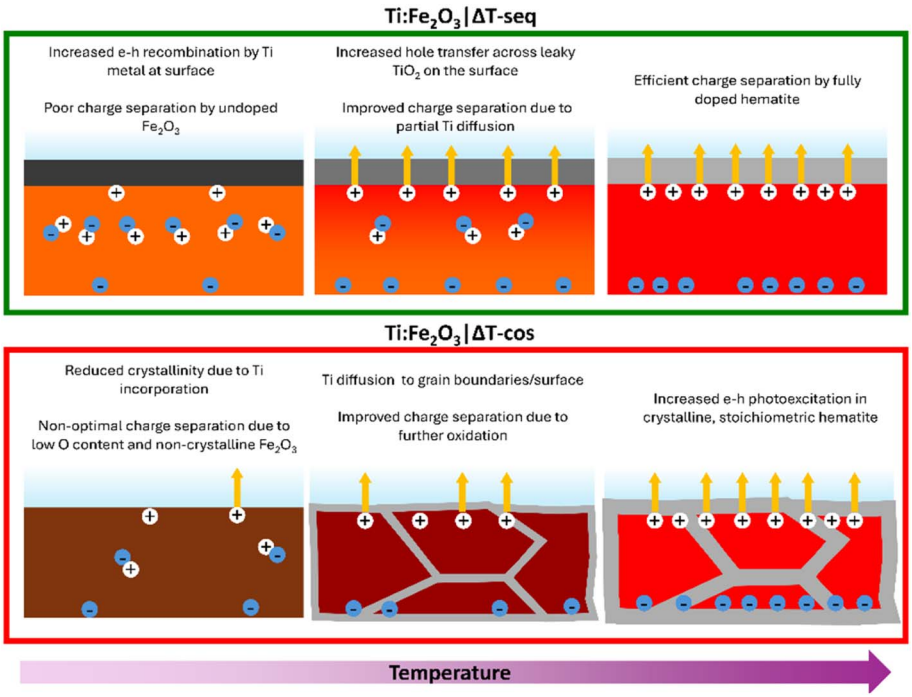

Fig. 8 Schematic representation of the changes in structure and how they reflect on the performance for the two types of temperature gradient samples. The charge separation efficiency is represented by the number of separated electron–hole couples, with the electrons (cyan) reaching the back contact at the bottom and the holes (white) the electrolyte at the top. The transfer efficiency is represented as the fraction of the holes accumulated at the interface that are transferred (gold arrows) to the solution. Absorption is represented by the total number of electron–hole couples. The color for the hematite film in the sequential sample (Ti:Fe_2O_3|Δ*T*-seq) evolves from orange (pristine hematite) to red (doped hematite), while the color gradient at intermediate temperatures represents the Ti diffusion profile, accompanied by an increase in charge separation. The titanium overlayer gets gradually oxidized passing from a darker gray to a lighter one, representative of titanium dioxide. In the co-sputtered sample (Ti:Fe_2O_3|Δ*T*-cos) instead, hematite starts brown at low *T*, symbolizing the inclusion of excess Ti, which induces low crystallinity and partly reduces Fe. At high *T*, the color of the hematite layer matches the one for Ti:Fe_2O_3|Δ*T*-seq, due to the similar structure and doping content. Here, excess Ti segregates at the grain boundaries, forming a fully oxidized (light gray) layer of increasing thickness as temperature rises.

j_G is still very low. In contrast, on Ti:Fe_2O_3|Δ*T*-cos, where Ti atoms are already incorporated within the film during deposition, j_G rises at much lower annealing temperatures (>450 °C). Interestingly, Ti:Fe_2O_3|Δ*T*-cos exhibits limited crystalline character in this intermediate temperature regime, while Ti:Fe_2O_3-|Δ*T*-seq is already quite crystalline at low temperature. As already discussed, this suggests that the crystallinity is a secondary factor in determining performance and might contribute to it by increasing absorbance at higher temperatures in Ti:Fe_2O_3|Δ*T*-cos. Even if Ti is already incorporated in the bulk, j_G of Ti:Fe_2O_3|Δ*T*-cos increases with annealing temperature. In the low to intermediate temperature range, this change appears connected with increasing oxidation. In fact, XAS measurements indicate that at low temperature, Ti is partially present in the ilmenite phase $FeTiO_3$, which contains Fe^{2+}, a lower oxidation state compared to Fe^{3+} of hematite. This is due to the use of a metallic Ti target in the co-sputtering and to the lower electronegativity of Ti compared to Fe. Indeed, under low-temperature annealing conditions, where oxygen from the atmosphere has not fully infiltrated the film, O atoms may preferentially bind titanium, resulting in the partial reduction of iron. As annealing temperature increases full oxidation into hematite and TiO_2 takes place, as shown by XAS. In Ti:Fe_2O_3|ΔTi j_G increases with increasing Ti amount, suggesting that the dopant concentration increases even if all regions nominally contain enough Ti to reach the maximum solubility of about 4% Ti/(Ti + Fe) detected by TEM. Therefore, the amount of Ti atoms that diffuse inside depends on the Ti layer thickness. This can be explained considering that in the regions where the Ti layer is thinner, almost all Ti atoms are rapidly oxidized to TiO_2 during high temperature annealing.

On the other hand, the charge transfer efficiency is closely linked to redox processes at the semiconductor/electrolyte interface and is strongly influenced by changes in surface structure. In the Ti:Fe_2O_3|Δ*T*-seq sample, the transfer efficiency remains low up to 600 °C, then exhibits a sharp increase and reaches a maximum at ~720 °C before declining. In this sample, dark CVs reveal a cathodic peak (Fig. S21) that exhibits a linear scan rate–current relationship (Fig. S22), indicating a surface-confined process. Since the height of the peak decreases with increasing annealing temperature, it can be ascribed to trap states within sub-stoichiometric, Ti-containing oxides that are progressively oxidized. Therefore, we suggest that the initial improvement of the transfer efficiency with increasing annealing temperature arises from a decreasing concentration of surface trap states induced by oxidation. This

raises the transfer efficiency from 5%, which is well below the 50% of bare hematite (Fig. 4a, point at 0% Ti), to about 80% at 720 °C. At this point, surface oxidation is almost completed and the better transfer efficiency compared to bare hematite can be due to passivation of hematite surface states by the Ti-containing overlayer. Nevertheless, it appears that full oxidation does not benefit the transfer efficiency, which decreases by annealing at higher temperatures down to the level of bare hematite. Therefore, the existence of a maximum in the transfer efficiency appears coupled to an optimal degree of surface oxidation (Fig. 8). In fact, the presence of residual Ti^{3+} cations is known to facilitate hole transport through the TiO_2 layer, circumventing the problem that its valence band lies below that of hematite. This is the mechanism behind "leaky TiO_2" layers, which are used as protective coatings that allow the transfer of minority carriers to the electrolyte.[35]

In Ti:Fe_2O_3|Δ*T*-cos, the transfer efficiency at low annealing temperatures is about 30%, *i.e.* well above the afore-mentioned 5% of Ti:Fe_2O_3|Δ*T*-seq. This difference can be explained by the absence of a sub-oxidized Ti-containing layer on the surface. Indeed, no cathodic peak is detected for Ti:Fe_2O_3|Δ*T*-cos in dark CVs (Fig. S21). Nonetheless, the transfer efficiency increases up to 500 °C, after which it remains almost constant within the uncertainties. This increase may be due to a restructuring of the surface upon annealing. Interestingly, the transfer efficiency never attains the maximum value of about 80% observed in Ti:Fe_2O_3|Δ*T*-seq. In order to understand this difference, we point out that excess Ti atoms expelled from the bulk are readily oxidized as they segregate at the surface. Therefore, the surface TiO_2 layer may not contain enough Ti^{3+} ions to efficiently conduct holes. On the other hand, after annealing at 750 °C, η_{trans} is the same for the two types of samples and is also not significantly different from the one for Ti:Fe_2O_3|Δ*T*-cos at 550 °C. This similarity exists in spite of the different Ti local structures revealed by XAS (see Table S2), characterized by different phase abundances (TiO_2 polymorphs and ilmenite $FeTiO_3$). Indeed, different Ti-rich surface phases have been reported for Ti-modified hematite, including ilmenite,[20] pseudobrookite[21] and rutile.[36]

Concerning Ti:Fe_2O_3|ΔTi, the addition of Ti on the surface initially enhances the transfer efficiency with respect to bare hematite. However, when the layer becomes too thick, the transfer efficiency declines, likely due to increased resistance within the titania layer, which hinders effective charge transfer to the electrolyte.

Conclusions

In this study, we employed combinatorial synthesis and high-throughput measurements to investigate the influence of Ti doping and annealing temperature on the photoelectrochemical performance of hematite photoanodes. Indeed, by combining gradient doping and temperature profiling with IMPS, XRD, TEM, and XAS analyses, we were able not only to optimize these fabrication parameters, but also to shed light on the role of titanium in enhancing sputtered hematite films.

Our results clearly demonstrate that Ti contributes to improved photoelectrochemical activity *via* two distinct mechanisms: by modifying surface properties, either through catalytic enhancement or passivation of recombination-prone surface states, and by acting as a substitutional dopant that improves charge separation efficiency. This happens regardless of how Ti is introduced, whether by introducing it on the surface as in Ti:Fe_2O_3|Δ*T*-seq and Ti:Fe_2O_3|ΔTi samples or co-deposited throughout the film as in Ti:Fe_2O_3|Δ*T*-cos. Indeed, the use of two different strategies for Ti incorporation in hematite, which at high temperature show a remarkably similar structure and performance, but require different temperatures to kickstart their photoactivity, proves that Ti atoms must be in the bulk of hematite to improve the charge separation efficiency. Our analysis also explains why going beyond an optimal amount of Ti decreases the performance: excess titanium accumulating on the surface forms a layer of TiO_2 which can be neutral or even beneficial for intermediate thicknesses, but can hinder charge transfer if too thick.

Overall, our study underscores that titanium's ability to improve hematite performance stems not from a single mechanism, but from a nuanced balance of surface and bulk effects. These findings also highlight the strength of high-throughput methodologies in not only accelerating materials optimization, but in revealing complex structure–function relationships that would be challenging to identify through conventional approaches.

Author contributions

Marco Salvi: conceptualization, data curation, formal analysis, investigation, methodology, software, supervision, visualization, writing – original draft. Alberto Piccioni: conceptualization, methodology, resources, software, supervision, writing – review and editing. Nicola Gilli: investigation, resources. Alessandro Puri: investigation, formal analysis. Federico Boscherini: writing – review and editing. Raffaello Mazzaro: conceptualization, formal analysis, funding acquisition, investigation, project administration, supervision, visualization, writing – review and editing. Luca Pasquini: conceptualization, funding acquisition, project administration, writing – review and editing.

Conflicts of interest

The authors declare no conflict of interest.

Data availability

The data supporting the findings of this study are available within the article and its SI. The SI contains further details on the preparation of the samples, a description of the scanning flow photoelectrochemical cell, an explanation of the DRT fitting algorithm and several plots and images that are commented in the article. Additional datasets and raw data that support this work are available from the corresponding author

upon reasonable request. Supplementary information is available. See DOI: https://doi.org/10.1039/d5ta04174k.

Acknowledgements

We acknowledge ESRF and the LISA beamline. The data at LISA were collected under the In House Research program during experiment IH-MA-474. L. P. acknowledges the National Recovery and Resilience Plan (NRRP), Mission 4 Component 2, Investment 1.3, Call for tender No. 1561 published on 11.10.2022 by the Italian Ministry of University and Research (MUR), funded by the European Union – NextGenerationEU – Project NEST: Network 4 Energy Sustainable Transition – CUP J33C22002890007. R. M. acknowledges financial support under the NRRP, Mission 4, Component 2, Investment 1.1, Call for tender No. 1409 published on 14.9.2022 by MUR, funded by the European Union – NextGenerationEU – Project Title EPiCX – CUP J53D23007710001.

Notes and references

1 M. Woodhouse and B. A. Parkinson, *Chem. Mater.*, 2008, **20**, 2495–2502.
2 M. Woodhouse, G. S. Herman and B. A. Parkinson, *Chem. Mater.*, 2005, **17**, 4318–4324.
3 S. K. Suram, L. Zhou, N. Becerra-Stasiewicz, K. Kan, R. J. R. Jones, B. M. Kendrick and J. M. Gregoire, *Rev. Sci. Instrum.*, 2015, **86**, 033904.
4 R. Gutkowski, C. Khare, F. Conzuelo, Y. U. Kayran, A. Ludwig and W. Schuhmann, *Energy Environ. Sci.*, 2017, **10**, 1213–1221.
5 T. F. Jaramillo, S. H. Baeck, A. Kleiman-Shwarsctein, K. S. Choi, G. D. Stucky and E. W. McFarland, *J. Comb. Chem.*, 2005, **7**, 264–271.
6 R. Meyer, K. Sliozberg, C. Khare, W. Schuhmann and A. Ludwig, *ChemSusChem*, 2015, **8**, 1279–1285.
7 H. Kusama, N. Wang, Y. Miseki and K. Sayama, *J. Comb. Chem.*, 2010, **12**, 356–362.
8 S. Kumari, L. Helt, J. R. C. Junqueira, A. Kostka, S. Zhang, S. Sarker, A. Mehta, C. Scheu, W. Schuhmann and A. Ludwig, *Int. J. Hydrogen Energy*, 2020, **45**, 12037–12047.
9 L. Zhou, Q. Yan, A. Shinde, D. Guevarra, P. F. Newhouse, N. Becerra-Stasiewicz, S. M. Chatman, J. A. Haber, J. B. Neaton and J. M. Gregoire, *Adv. Energy Mater.*, 2015, **5**, 1500968.
10 M. Nowak, R. Gutkowski, J. Junqueira, W. Schuhmann and A. Ludwig, *Z. Phys. Chem.*, 2020, **234**, 835–845.
11 L. Zhou, D. Guevarra and J. M. Gregoire, *J. Phys.: Energy*, 2022, **4**, 044001.
12 S. Kumari, J. R. C. Junqueira, W. Schuhmann and A. Ludwig, *ACS Comb. Sci.*, 2020, **22**, 844–857.
13 C. J. Metting, J. K. Bunn, J. Fadimba, E. Underwood, Y. Zhu, G. Koley, T. Crawford and J. Hattrick-Simpers, *Rev. Sci. Instrum.*, 2013, **84**, 036111.
14 Y. Han, B. Matthews, D. Roberts, K. R. Talley, S. R. Bauers, C. Perkins, Q. Zhang and A. Zakutayev, *ACS Comb. Sci.*, 2018, **20**, 436–442.
15 M. Gilzad Kohan, R. Mazzaro, V. Morandi, S. You, I. Concina and A. Vomiero, *J. Mater. Chem. A*, 2019, **7**, 26302–26310.
16 S. Berardi, V. Cristino, C. A. Bignozzi, S. Grandi and S. Caramori, *Inorg. Chim. Acta*, 2022, **535**, 120862.
17 G. Wang, Y. Ling, D. A. Wheeler, K. E. N. George, K. Horsley, C. Heske, J. Z. Zhang and Y. Li, *Nano Lett.*, 2011, **11**, 3503–3509.
18 S. Shen, C. X. Kronawitter, D. A. Wheeler, P. Guo, S. A. Lindley, J. Jiang, J. Z. Zhang, L. Guo and S. S. Mao, *J. Mater. Chem. A*, 2013, **1**, 14498–14506.
19 O. Zandi, B. M. Klahr and T. W. Hamann, *Energy Environ. Sci.*, 2013, **6**, 634–642.
20 S. Berardi, J. Kopula Kesavan, L. Amidani, E. M. Meloni, M. Marelli, F. Boscherini, S. Caramori and L. Pasquini, *ACS Appl. Mater. Interfaces*, 2020, **12**, 47435–47446.
21 D. Monllor-Satoca, M. Bärtsch, C. Fàbrega, A. Genç, S. Reinhard, T. Andreu, J. Arbiol, C. Markus Niederberger and J. R. Morante, *Energy Environ. Sci.*, 2015, **8**, 3242.
22 K. D. Malviya, D. Klotz, H. Dotan, D. Shlenkevich, A. Tsyganok, H. Mor and A. Rothschild, *J. Phys. Chem. C*, 2017, **121**, 4206–4213.
23 P. Zhang, A. Kleiman-Shwarsctein, Y. S. Hu, J. Lefton, S. Sharma, A. J. Forman and E. McFarland, *Energy Environ. Sci.*, 2011, **4**, 1020–1028.
24 A. T. Paradzah, K. Maabong-Tau, M. Diale and T. P. J. Krüger, *Phys. Chem. Chem. Phys.*, 2020, **22**, 27450–27457.
25 J. He and B. A. Parkinson, *ACS Comb. Sci.*, 2011, **13**, 399–404.
26 Y. Ma, P. S. Shinde, X. Li and S. Pan, *ACS Omega*, 2019, **4**, 17257–17268.
27 F. d'Acapito, G. O. Lepore, A. Puri, A. Laloni, F. La Manna, E. Dettona, A. De Luisa and A. Martin, *J. Synchrotron Radiat.*, 2019, **26**, 551–558.
28 L. Zhou, A. Shinde, D. Guevarra, M. H. Richter, H. S. Stein, Y. Wang, P. F. Newhouse, K. A. Persson and J. M. Gregoire, *J. Mater. Chem. A*, 2020, **8**, 4239–4243.
29 A. Piccioni, P. Vecchi, L. Vecchi, S. Grandi, S. Caramori, R. Mazzaro and L. Pasquini, *J. Phys. Chem. C*, 2023, **127**, 7957–7964.
30 W. W. Gärtner, *Phys. Rev.*, 1959, **116**, 84–87.
31 W. J. Albery and P. N. Bartlett, *J. Electrochem. Soc.*, 1983, **130**, 1699–1706.
32 S. Kment, P. Schmuki, Z. Hubicka, L. Machala, R. Kirchgeorg, N. Liu, L. Wang, K. Lee, J. Olejnicek, M. Cada, I. Gregora and R. Zboril, *ACS Nano*, 2015, **9**, 7113–7123.
33 J. Li, H. Chen, C. A. Triana and G. R. Patzke, *Angew. Chem., Int. Ed.*, 2021, **60**, 18380–18396.
34 M. I. Pownceby, M. J. Fisher-White and V. Swamy, *J. Solid State Chem.*, 2001, **161**, 45–56.
35 M. T. McDowell, M. F. Lichterman, A. I. Carim, R. Liu, S. Hu, B. S. Brunschwig and N. S. Lewis, *ACS Appl. Mater. Interfaces*, 2015, **7**, 15189–15199.
36 I. Carrai, R. Mazzaro, E. Bassan, G. Morselli, A. Piccioni, S. Grandi, S. Caramori, P. Ceroni and L. Pasquini, *Sol. RRL*, 2023, **7**, 2300205.

